

Conduction band resonant states absorption for quantum dot infrared detectors operating at room temperature

Stefano Vichi^{1,*}, Shigeo Asahi², Sergio Bietti¹, Artur Tuktamyshev¹,

Alexey Fedorov³, Takashi Kita², and Stefano Sanguinetti¹

¹ *L-NESS and University of Milano-Bicocca,*

Department of Materials Science, Via Cozzi 55, Milano, Italy

² *Department of Electrical and Electronic Engineering,*

Kobe University, 1-1 Rokkodai, Nada, Kobe 657-8501, Japan

³ *L-NESS and CNR-IFN, via Anzani 42, 22100 Como, Italy*

* *corresponding author email: stefano.vichi@unimib.it*

(Dated: July 29, 2024)

Long Wavelength infrared devices, despite growing interest due to a wide range of applications in commercial, public, and academic sectors, are still struggling to achieve significant improvements over well-established technologies like HgCdTe detectors. Devices based on quantum nanostructures remain non competitive due to unresolved drawbacks, the most significant being the need to cool down to liquid nitrogen temperatures to improve the signal-to-noise ratio. In this work, we demonstrate an innovative solution to surpass the current generation of quantum dot-based detectors by exploiting the absorption from quantum dot localized states to resonant states in the continuum, that is states in the semiconductor conduction band with an enhanced probability density in the quantum dot region. This unprecedented approach takes advantage of the unique properties of such states to massively enhance carrier extraction, allowing to overcome one of the most crucial drawbacks of quantum dot-based infrared detectors. This innovative solution is discussed here from both theoretical and experimental perspectives. The measured room temperature operation with high detectivity demonstrates that exploiting resonant states absorption in quantum dots offers the long-sought solution for the next generation of infrared photodetectors.

Keywords: room temperature, quantum engineering, quantum dots

I. INTRODUCTION

The advancement of long wavelength infrared (LWIR) detectors for imaging relies heavily on the realization of an improved generation of sensors. These innovative sensors aim to offer photodetectors with improved features, including a higher pixel count, high frame rates, superior thermal resolution, and the ability to operate at room temperature, thus having a groundbreaking impact on all domains, such as earth remote observation [1, 2], automotive[3], imaging[4] and military defense.

Currently, four primary semiconductor based photodetector technologies are being developed in the LWIR spectrum: HgCdTe photodiodes, quantum well infrared photodetectors (QWIP), quantum dot infrared photodetectors (QDIP), and antimonide-based type II superlattice photodiodes. Among these, bulk HgCdTe stands out as the most mature technology, offering superior performances and a broad, adjustable detection spectrum. On the other hand, the latter three technologies leverage quantum heterostructures based on III-V semiconductor materials, facilitating their integration with existing technology platforms[5]. Demonstrations of monolithic silicon integration for III-arsenic (As) and III-antimony (Sb) materials, fundamental for the implementation of these three technologies into ac-

tual devices, have been successful[6–11]. Among all, QDIP are gaining attention as a promising alternative, attributed to their precise control over transition energies due to three-dimensional carrier confinement and the lack of restrictive selection rules, which currently limit the broader adoption of QWIP technology.

On the paper, QDIPs represent a significant advancement in the field of LWIR detection, offering a range of attractive capabilities: i) high sensitivity, capable of detecting low levels of infrared radiation, ii) engineered flexibility which allow to detect infrared radiation across a wide range of wavelengths by adjusting the size and composition of the Qds, iii) low dark current and low noise characteristics, resulting in improved signal-to-noise ratios compared to other infrared detectors, iv) can be fabricated using semiconductor well established processing techniques. This makes them suitable for various applications, including night vision, thermal imaging, and environmental monitoring. [12]. Despite their promising features, QDIPs also present several drawbacks that currently limit their performance and practical application. One of the primary challenges associated with QDIP technology is the relatively low operating temperature. Currently, QDIPs often require cooling to very low temperatures to achieve optimal performance, which increases the complexity and cost of the detection systems. This cooling requirement is due to the thermal activation of carriers in the quantum

dots, which can lead to increased noise and decreased detector sensitivity at higher temperatures. Another limitation is the dark current, which is the current that flows through the photodetector even in the absence of light. In QDIPs, the presence of defects and the complex structure of the quantum dots can contribute to a higher dark current, thereby reducing the signal-to-noise ratio and impairing the detector's overall performance. Additionally, the quantum efficiency, which is a measure of how effectively the photodetector converts incoming photons into electrical signals, can be lower in QDIPs compared to other infrared detection technologies. This is partly due to the inherent properties of quantum dots, due to the relatively low density of absorbers (the QDs) and to issues related to carrier escape and recombination within the dots. While QDIPs offer the potential for high-resolution and tunable infrared detection, these drawbacks highlight the need for ongoing research and development to overcome the challenges and fully realize the technology's capabilities in practical applications.

With this work we are opening a new path for QDIP detection, which exploits the unique properties of resonant states absorption in quantum dots. This approach, which was never explored, allowed us to demonstrate a photodetector with a high room temperature detectivity in the LWIR spectral region. Our detector design specifically incorporates a hybrid structure comprising quantum dots and a quantum well, both made of the same material. This mixed structure results in hybrid QD-QW states, which can be engineered to enhance the extraction efficiency of photoexcited carriers while maintaining a significant wavefunction overlap with the QD ground state. Besides, this design provides the necessary control over quantum states and their carrier occupation to be able to selectively enhance or suppress electron thermalization channels, allowing to engineer carrier dynamics and the detection process in an unprecedented way. Here, we present the design principles, fabrication techniques, and experimental results of our novel quantum-based LWIR detector.

II. NANOSTRUCTURE DESIGN

Improving the current generation by LWIR at room temperature of QDIPs requires the a deep analysis of the design of the processes involved and of their weak points with the final goal of overcoming their limitations or limiting their impact on detection performances.

The typical QDIP device structure is illustrated in Figure 1 a. The QDIP is a photoresistive detector, where LWIR light is detected through an increase in device current due to photon absorption. This absorption causes transitions between the ground and excited states of electrons confined within the quantum dots

(QDs). The standard electronic configuration is an n-i-n heterostructure. The active zone, embedded in the intrinsic region of the QDIP, consists of multiple layers of self-assembled QDs within a barrier layer with a larger bandgap, ensuring carrier confinement in three dimensions. The processes involved in QD intraband detection are schematized in Figure 1 b, providing a visual representation of the electron dynamics in the QDIP. When LWIR radiation strikes the QDIP, photons with energy matching the energy difference between the QDs confined states are absorbed. This absorption excites the electrons present in the QDs, which are introduced by intentional doping or are captured, and subsequently thermalized, from the barrier conduction band, from a lower energy state (often the ground state) to a higher energy state (an excited state) within the QDs. The specific energy levels of the quantum dots can be engineered to target different LWIR wavelengths, making QDIPs versatile for various IR detection applications. Once the electrons are excited to higher energy states, the electrons are promoted to the conduction band of the surrounding semiconductor material, by tunneling or thermionic processes, and are then collected by electrodes, creating a measurable photocurrent. Each process is indicated, in Figure 1 b, by an arrow, with its color (from red to green) and size (from small to large) indicating an increasing probability of the transition respectively.

Let us begin by analyzing the critical process of carrier dynamics as depicted in Figure 1 b. The QDIP signal is generated through a series of processes: photon absorption, extraction of the photoexcited electron from the quantum dot (QD) into the conduction band, and finally, collection at the device electrodes. Competing with photon absorption is the thermally promoted carrier escape process, which is typically the dominant mechanism at room temperature in standard QDIP designs and adds up to the dark current generated by other areas of the device. For the QD to remain active after the initial photon absorption, the QD ground state must be refilled by electrons from the barrier conduction band through capture and thermalization processes. The efficiency of this combined process contributes to both photocurrent intensity and frame rate. In this regard, the small carrier capture cross section of QDs [13–15], caused by their limited size, is certainly a weak point of QDIPs. The color code in Figure 1 b, indicates the limiting processes (red color) in actual QDIP quantum device design.

We begin our nanostructure design process by identifying corrective measures to mitigate the processes that limit QDIP performance at room temperature. The process of QD refilling, which involves the combination of carrier capture and thermalization to the ground state, has been identified in the literature as a limiting factor for QDIP sensitivity [16]. In fact, if the electrons

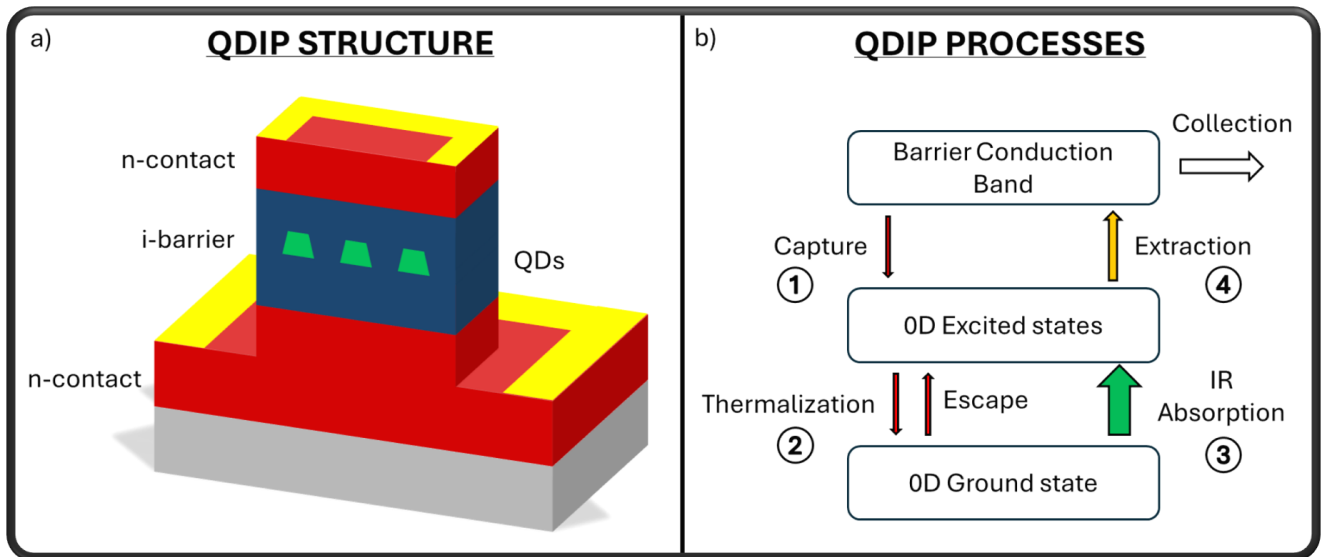


Figure 1. a) Typical QDIP device structure, made of an n-i-n heterojunction. One or more QD layers are embedded in the intrinsic barrier region with a larger band gap. b) Schematics of the electron dynamics processes in the QDIP. The numeric labels indicate the order of the detection steps. Each process is represented by an arrow which indicates the transition direction, with its color (from red to green) and size (from small to large) indicating an increasing transition probability.

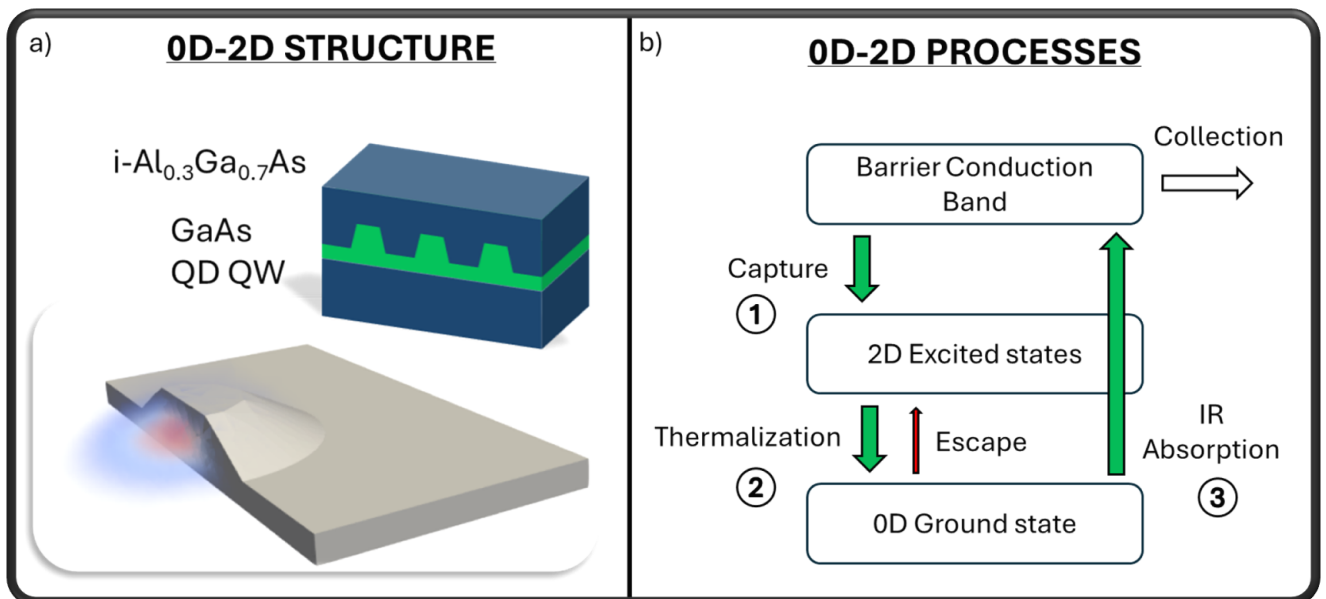


Figure 2. a) Representation of the 0D-2D nanostructure, with the drawing of the 0D ground state b) Schematics of the electron dynamics processes in the 0D-2D structure. The numeric labels indicate the order of the detection steps. Each process is represented by an arrow which indicates the transition direction, with its color (from red to green) and size (from small to large) indicating an increasing transition probability.

that leave the QD due to photon absorption or thermal excitation are not immediately replaced by electrons captured from the conduction band, the QD remains inactive, preventing further absorption.

In the literature, the capture probability drawback

has been addressed in two ways: by increasing the number of free carriers in the barrier which can be captured (e.g. by using a pumping laser [17–19]) or by increasing the capture probability of the QDs by embedding them in a QW of a material with a gap intermedi-

ate between the QDs and the barrier [20]. The latter strategy, named dot-in-a-well (DWELL) device structure [21, 22], favours the carrier injection into the QDs by their spatial confinement in the QW. Still carrier scattering at the interface and strain induced potential barriers present in the DWELL design hinders a fast and efficient carrier capture in the QDs.

Here, the use of droplet epitaxy for QD fabrication - a self-assembling technique in an MBE environment based on the sequential deposition of group III and group V elements that does not rely on strain to promote QD formation [23, 24] — allows us to overcome these drawbacks. It is also extremely flexible and powerful when it comes to quantum state engineering, as it allows to obtain QDs with a narrow size distribution [25], with an excellent control on their shape and size [26, 27] and without restrictions on surface orientation [28–30]. This technique enables the combination of a quantum well (QW) with quantum dots (QDs) made of the same material, as depicted in figure 2 [31]. In particular the barrier material is an AlGaAs ternary alloy and the QW/QD nanostructure is made by GaAs. The resulting system is a thickness-modulated QW, with the 3D modulation controlled by the shape and size of the QDs. This thickness-modulated QW possesses unique and complex electronic states that differ significantly from those in conventional QWs. The varying thickness creates regions where quantum confinement is significantly altered due to the reduced importance of the kinetic term in the electronic Hamiltonian in the thicker regions. As a result, electrons can become localized in regions with a reduced kinetic energy, leading to the presence of discrete QD-like energy levels at the bottom of the energy ladder. The higher-lying energy states remain QW-like. This forms a hybrid QW/QD nanostructure in which the electronic states gradually transform from QD-like to QW-like states, with no distinct interfaces or potential barriers. A detailed calculation of such a hybrid structure is reported in Section III.

The use of a hybrid 0D-2D nanostructure not only improves the injection of carriers into the quantum dots (QDs) but also allows for extensive engineering flexibility. In fact, four independent structural parameters can be finely tuned in such systems, enabling precise control of the carrier processes within the nanostructure. These parameters are: (i) barrier height, (ii) quantum well (QW) thickness, (iii) QD lateral size, and (iv) QD height.

In a QDIP or a DWELL device, after the electrons are captured in a QD excited state, their thermalization to the QDs ground state is hindered by the phonon bottleneck effect [14, 32–34]. The discrete density of states of QDs slows down this process as only transitions with an energy close to the one of optical phonons are allowed. This points out the inefficient thermalization process typical of QDs, which severely limits their ability to fill

their ground state. It is possible to avoid such drawback by making the electronic state ladder with energy differences between the states nearly matching the optical phonon energy (around 36 meV in GaAs) thus increasing the electron-phonon interaction [32]. Typically, in InAs/InGaAs QD systems the electron-phonon interaction is strong enough to remove the phonon bottleneck as clearly demonstrated by the pinning of the quasi-Fermi energy in QD based intermediate band solar cells [35].

However, limiting the electron-phonon interaction helps suppress carrier thermal escape, which should significantly reduce the dark current, especially at higher temperatures. Therefore, the phonon bottleneck represents both an advantage and a disadvantage for QDIP performance. To benefit from it while avoiding its drawbacks, it is necessary to design the system to use different processes for carrier thermalization and thermal escape. The solution we propose again relies on the properties of the QW/QD heterostructure, which allows to engineer carrier dynamics in an unprecedented way with the objective of enabling alternative thermalization channels which are not relevant in QDIP and which do not involve the reduction of the electron-phonon interaction. In this regard, it is worth noting that the QW acts as a carrier reservoir for the QDs, thanks to the large density of state which can accommodate a large number of captured electrons. The absence of internal potential barriers compared to DWELL design leads to the first significant difference with our engineered nanostructure. As can be seen from the schematic drawing of figure 3 a, thanks to our design the excited states have mixed 0D-2D nature, with a large wavefunction overlap with the 0D ground state. This feature, combined with the ability to accumulate a large number of carriers in a confined space, allows to increase significantly the probability of carrier-carrier scattering (i.e. Auger scattering), creating an alternative thermalization channel [36, 37]. Despite the possibility to have this process also in DWELL, the presence of an interface between QDs and QW combined with the two different confining potential results in a lower overlap of the states. As required, the presence of thermalization channels through carrier-carrier interaction does not affect the escape probability from the QDs ground state, maintaining the positive effects of phonon bottleneck.

Once the ground state of the QDIP is filled, electrons are able to absorb LWIR radiation by transitioning to an excited 0D confined state, with a probability determined by their optical matrix elements. This is another process in which QDIP shines, thanks to the large overlap between confined states. Once excited to a high-energy confined state, the electrons need to overcome a potential barrier before being collected at the contacts. This process can be achieved either by thermionic emission or by tunneling. Although these mechanisms are

facilitated by temperature and bias applied to the device, their efficiency is limited and strongly depends on the position of the excited state with respect to the conduction band energy [38]. Here our quantum design of the QDIP takes a different approach. As can be seen from the right panel of figure 2, we have designed the 0D-2D nanostructure in such a way that the transition occurs to a resonant state in the conduction band. This has a tremendous impact on the extraction probability of photoexcited carriers, as resonant states are conduction band states, thus eliminating completely carrier extraction issues. The conduction band resonant states, which originate from the interference caused by the confining potential discontinuities on the continuum states, are well known in literature for 2D systems [39–43] and are typically applied to resonant photonic devices such as lasers, sensors and filters [44–46]. In particular, due to the mixed nature of the QD-QW system devised in this study, here the resonant states in the conduction band are strongly mixed with the 0D confined states, thus being able to generate 0D-2D resonant states with a strong localization in the QD region resulting in large optical matrix elements for optical transitions with the QD-like ground state. This is the first time in which optical transitions to resonant states are used for IR detection in QDIPs.

III. QUANTUM PROPERTIES

A more detailed insight on the quantum properties of the 0D-2D nanostructure can be understood by looking at the calculated conduction band density of states, based on the dimensions of our QDs, shown in figure 3b. Here, the confined state energies are expressed with respect to the bottom of the conduction band. The low energy states are well separated while at higher energies the states form a continuous DOS with a step-like shape. These high-energy 2D states allow for a large carrier capture efficiency, act as a reservoir to fill the nanostructures ground state and allow to improve significantly the thermalization efficiency through carrier-carrier scattering [36, 37].

The resonant states above the CB edge play a significant role in the absorption of the 0D-2D hybrid nanostructure. Indeed, the numerical calculations performed on the basis of the designed nanostructures (see section IV) show the presence of a few resonant states with the largest optical matrix elements for the intraband transition with the ground state. Figure 4 shows the probability density function of the ground state and the three states with the largest optical matrix elements (from left to right respectively). As expected, the ground state is an s-like 0D state as typically found in QDs. On the other hand, all the excited states show a mixed 0D-2D component and a strong localization in the central re-

gion corresponding to the QD location (see the lower panel of figure 4). These states have a transition energy with the ground state of 170 meV, 155 meV and 150 meV respectively, all of which are above the CB edge energy (138 meV). It is interesting to notice that none of these states has an s-like symmetry in the QD region but they all have a p-like symmetry, an expected consequence of the intraband transition selection rules under dipole approximation [47].

IV. DEVICE CHARACTERIZATION

In order to obtain absorption in the LWIR region, we designed the nanostructures with a QD height of 2.0 nm and a radius of 9.5 nm on top of a QW 1.1 nm thick. The material of the 0D-2D nanostructure was GaAs, while the barrier was made of $\text{Al}_{0.3}\text{Ga}_{0.7}\text{As}$.

The I-V curve of the device measured at room temperature is shown in figure 5. Remarkably, in our device the dark current is extremely low even compared to the low temperature measurements of QDIP [48–50], DWELL [51, 52] and QWIP [53]. We attribute the slight shift of the zero-current point to the asymmetries in the stack of the grown structure which may lead to spurious capacitive effects. The asymmetry in the structure is also responsible for the different behavior at large voltage.

Figure 6a shows the AFM image of the uncapped QDs grown on a QW of 1.1 nm thickness. The mean height is 2.0 ± 0.6 nm and the mean radius is 9.5 ± 3.1 nm, as obtained by fitting with a Gaussian function the histogram data of figure 6 b) and c) respectively. The calculated QD density is $7 \cdot 10^{10} \text{cm}^{-2}$. The details of the AFM measurements are described in section VIII D. We attribute the relatively large size dispersion to the low substrate temperature and high Ga flux used for QDs formation.

The optical properties of the QDs were investigated by photoluminescence (PL). Figure 7 a displays the temperature dependence of the normalized PL spectrum, with the logarithmic plot of the PL spectrum presented in figure 7 b. At 300 K, we observed an emission at the peak wavelength of 870 nm corresponding to 1.42 eV, which is attributed to the emission of GaAs. This emission intensifies and shifts to the shorter-wavelength side as the temperature decreases. When the temperature dropped below 45 K, the emission from GaAs was overwhelmed by a narrower-bandwidth emission, attributed to the exciton recombination in GaAs. The peak wavelength of the exciton emission was approximately 815 nm (1.52 eV) at 3.5 K. In addition, a distinct PL peak becomes evident with decreasing temperature at the wavelength of around 850 nm, appearing to be a combination of several peak PL emissions. These emissions originate from shallow impurity states due to

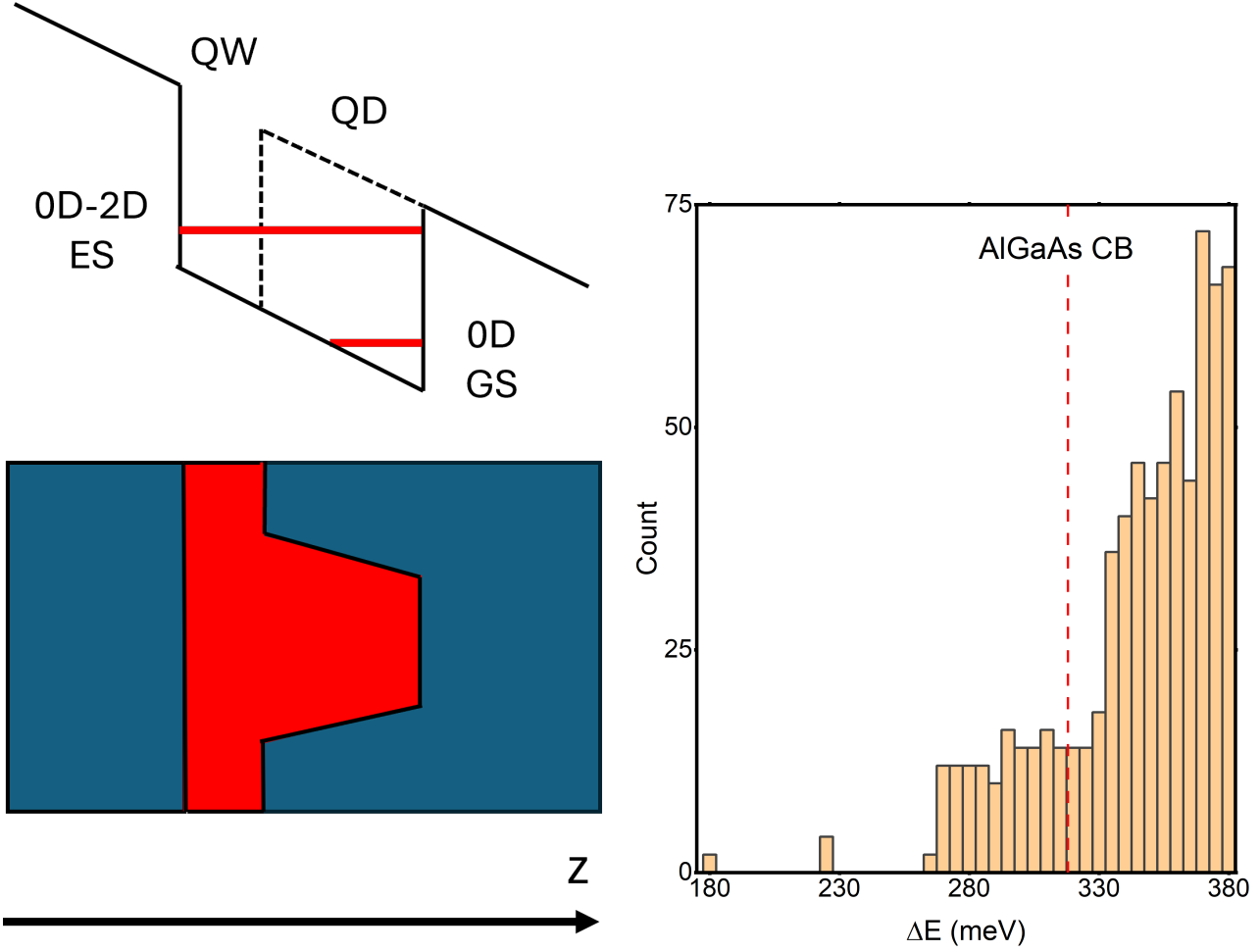


Figure 3. a) Schematized drawing of the ground state and excited confined energy levels in the 0D-2D nanostructure from where it can be intuitively understood the nature of the states. In particular, the ground state is zero dimensional while the excited states are mixed 0D-2D. b) Calculated electron density of states of the 0D-2D nanostructure, which demonstrates the claims on the confined states nature. The energies are reported with respect to the bottom of the GaAs conduction band. The dashed red line shows the energy of the $\text{Al}_{0.3}\text{Ga}_{0.7}\text{As}$ CB.

carbon, Si, or other contaminants in GaAs [54]. Furthermore, an emission around 730 nm appears at 200 K, becoming significant and shifting to a lower wavelength side as the temperature decreases. The peak wavelength was approximately 710 nm at 3.5 K. This peak is attributed to the ground-state emission of QDs, in agreement with the calculated value of 704 nm obtained from the numerical simulations. Moreover, a weak PL emission was observed at the wavelength of 630 nm (1.97 eV), originating from the $\text{Al}_{0.3}\text{Ga}_{0.7}\text{As}$ barrier layer. Figure 7 c shows the excitation intensity dependence of the PL spectrum at 4 K. The emissions from the QDs and the $\text{Al}_{0.3}\text{Ga}_{0.7}\text{As}$ barrier layer become more evident with increasing intensity. Specifically, for the emission of the QDs, the lower-wavelength emission becomes more evident with increasing intensity. This feature indicates a state-filling of the QDs.

Figure 8 shows the comparison between the simulated absorption spectrum (black line) and the measured spectrum at room temperature (red bars). As can be seen, there is a remarkable agreement between the simulations and the measurements. Indeed, the experimental results show that most of the absorption comes from shorter wavelengths than the transition from the GS to the CB edge, which confirms the theoretical prediction of an efficient absorption transition to resonant states in the conduction band. Remarkably, the main observed absorption peak is extremely narrow, lying in the $6\ \mu\text{m}$ - $7.3\ \mu\text{m}$ spectral window. It can be observed a second - less intense - absorption peak which lies between $8\ \mu\text{m}$ and $12\ \mu\text{m}$. Also in this case our simulations confirm the resonant nature of the excited state responsible for this transition. We measured a room temperature peak responsivity of $2 \cdot 10^{-4}\ \text{A/W}$ using the $6\ \mu\text{m}$

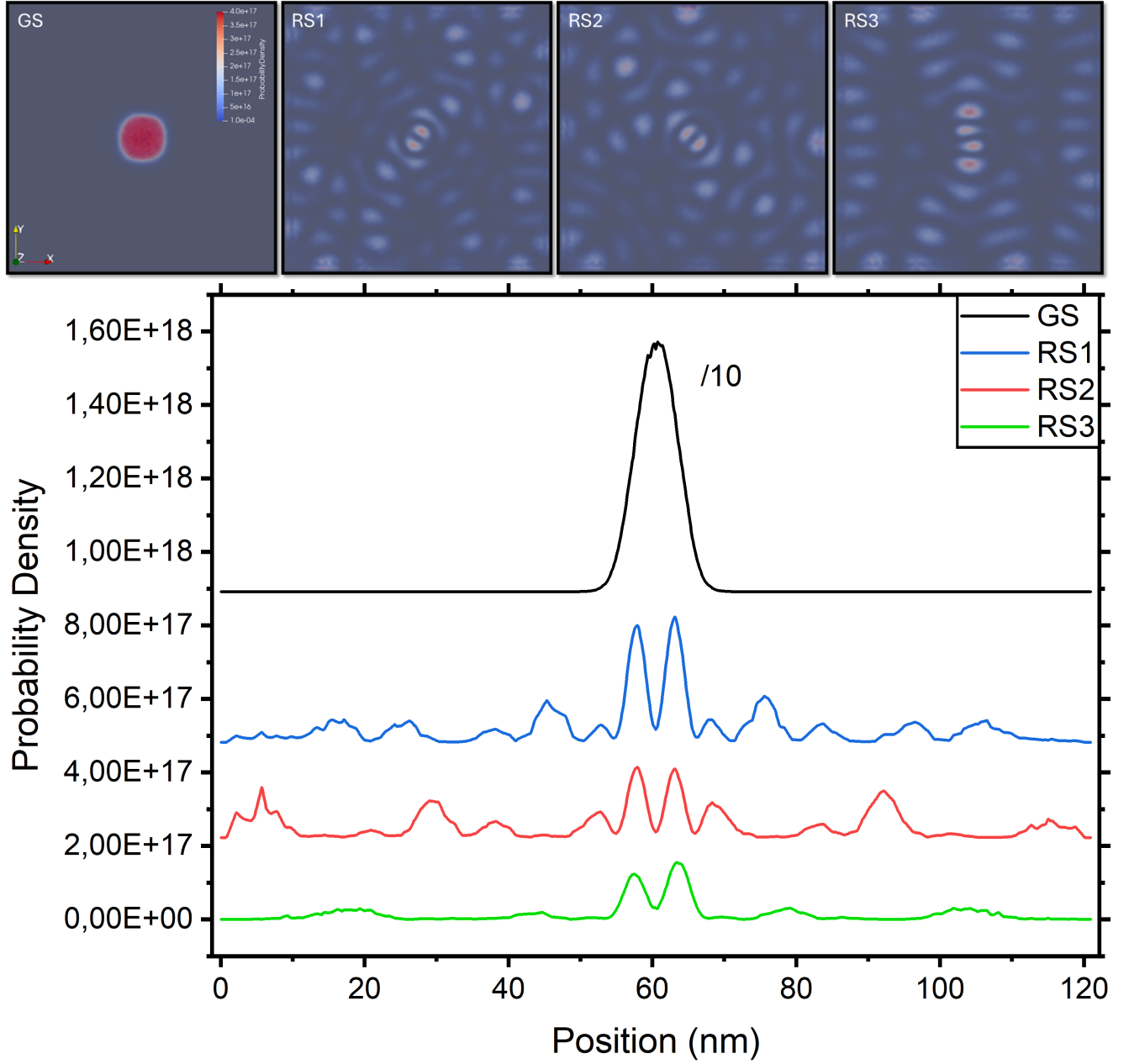


Figure 4. Electron wavefunction probability density of the ground state (GS) and the three excited resonant states with the largest optical matrix elements (RS1, RS2 and RS3 respectively). The transition energy with the ground state are $7.3 \mu\text{m}$, $8 \mu\text{m}$ and $8.3 \mu\text{m}$ respectively. The bottom panel shows the line plot of the wavefunction probability densities along the diagonal.

longpass filter at a bias of -4 V .

V. DISCUSSION

The presence of resonant states in the continuum was already discussed in literature [39–43] mostly related to QWs. Typically, the absorption spectrum involving

these states is very broad due to the large amount of closely-spaced states [39]. On the other hand, our results show a narrow main absorption peak located in the $6 \mu\text{m} - 7.3 \mu\text{m}$ region. We attribute this feature to the combination of having a QD-like ground state and the presence of hybrid 0D-2D states at high energies, with a strong localization in the QD region. To explain this, we can describe each quantum state as

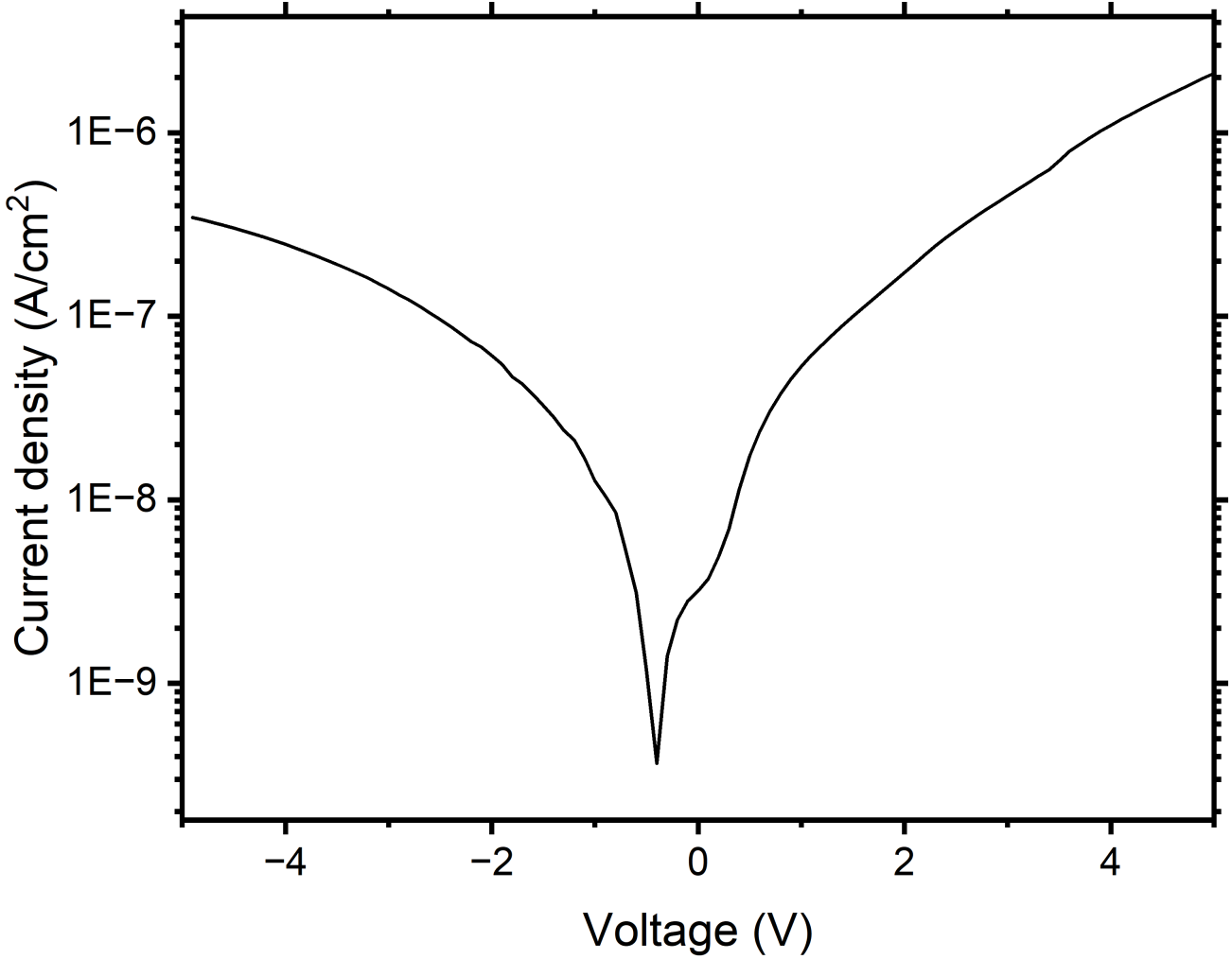


Figure 5. Room temperature I-V curve of the device.

a combination of an excited QD state and an excited QW state, with the quantum numbers of the two that are independent and determined by their total energy. Since the ground state of the system is a QD *s*-state, as can be seen from figure 4, the absorption selection rules depend on the 0D component of each state, as this is the only one with non-zero matrix elements with the ground state. Therefore, since the selection rules for intraband transitions under dipole approximation require that the difference in the principal quantum number between the transitioning states must be an odd number, only the states with a 0D component which is p-like are allowed, as confirmed by the simulations of figure 4. This causes a restriction in the number of states which can absorb light and therefore it limits the broadening of the absorption spectrum.

With the knowledge of the optical and electrical performance is then possible to evaluate a fundamental figure of merit, the specific detectivity (D^*). The detectiv-

ity is a parameter defined to characterize the capability of detecting photons of a given detector. This capability is described by the ratio between the signal level and the noise level. D^* can be calculated as follows

$$D^* = \frac{\sqrt{A\Delta f}}{NEP} \quad (1)$$

where A is the detector area, Δf is the bandwidth, and NEP is the noise equivalent power. This is defined as the input power required of the optical signal for the signal-to-noise ratio to be unity ($SNR = 1$). The NEP in a photodetector can be expressed as the ratio between the mean square noise current at an input optical power for which $SNR = 1$ and its responsivity. In QD-based photodetectors operating at high temperature, it can be assumed that the major contribution to the noise current comes from the blackbody radiation in the background (i.e. thermal noise) [55]. Therefore,

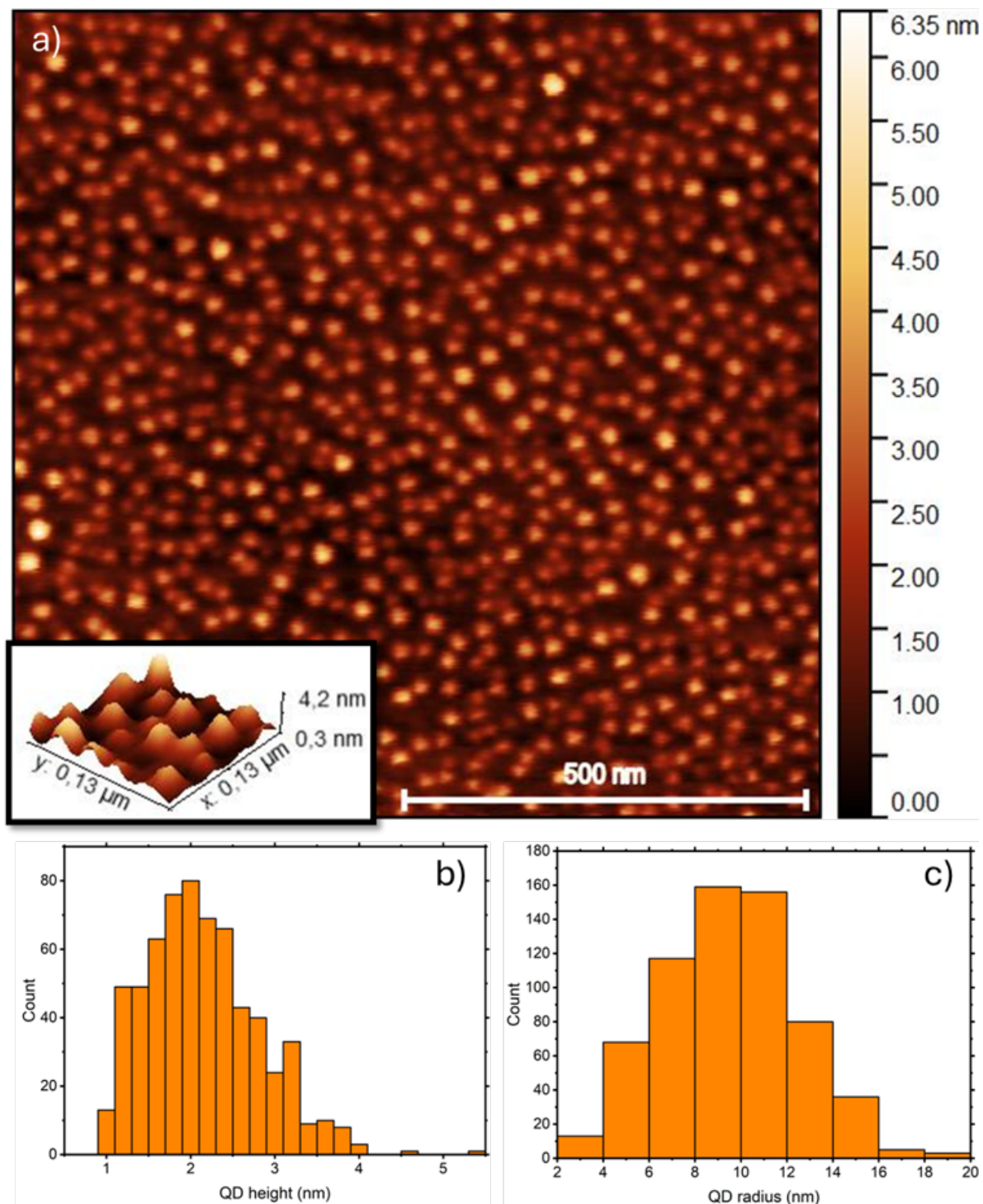


Figure 6. AFM image (a) and the obtained distribution of QD height (b) and radius (c). The mean QD height is 2.0 ± 0.6 nm and the mean QD radius is 9.5 ± 3.1 nm, with a dot density of $7 \cdot 10^{10} \text{ cm}^{-2}$.

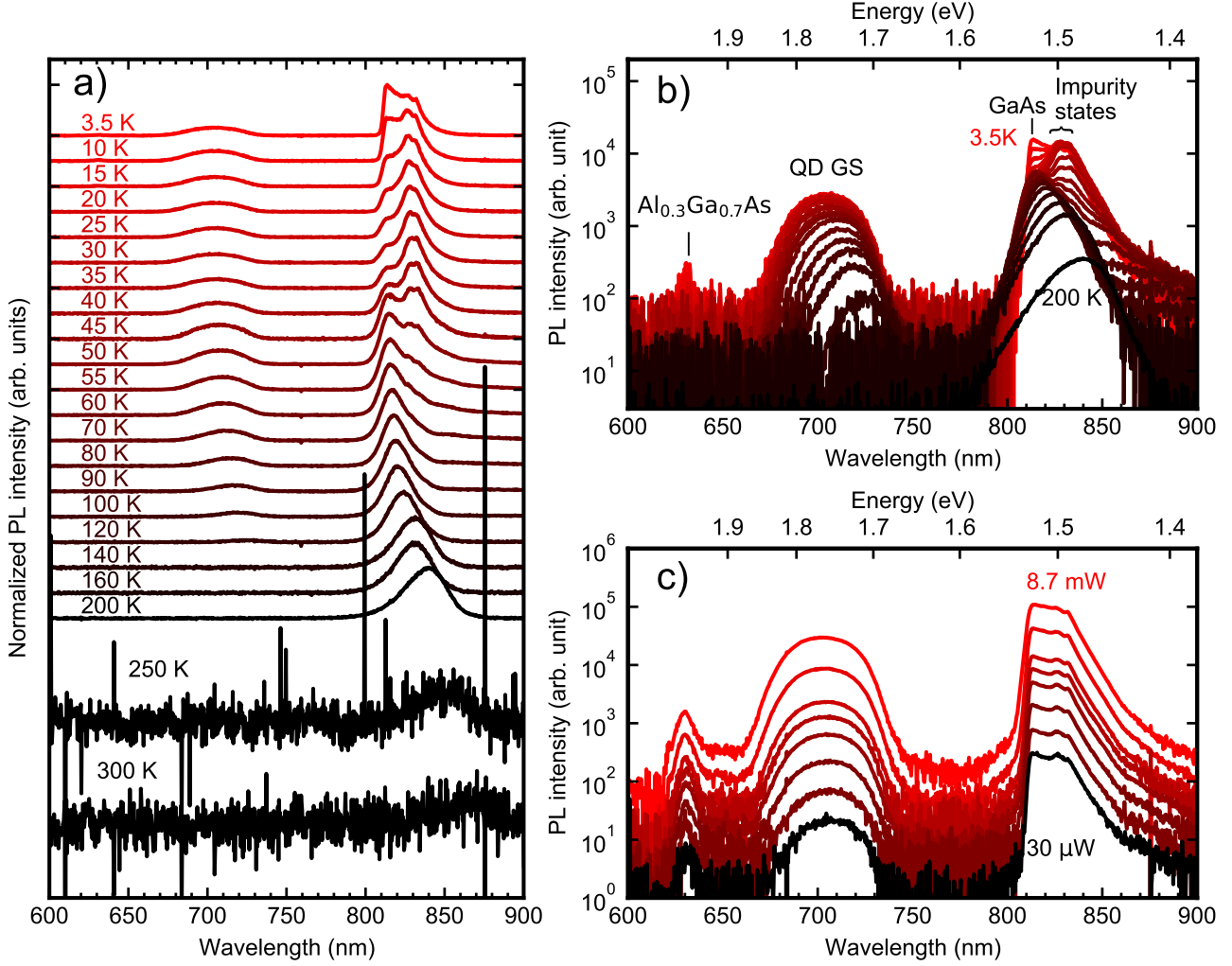


Figure 7. (a) Temperature dependence of normalized photoluminescence (PL) spectra. (b) Semi-logarithmic plot of figure 7 a). (c) Intensity dependence of the PL at 4 K.

the NEP is

$$NEP = \frac{1}{\mathcal{R}} \frac{\sqrt{4k_B T B}}{R} \quad (2)$$

where \mathcal{R} is the responsivity, k_B is the Boltzmann constant, T is the temperature, B is the bandwidth, and R is the resistance. The photodetectors shows a D^* of 9.8×10^9 cm Hz^{1/2}/W for an applied voltage of -4 V at $T = 300$ K. To our knowledge, this is the largest value reported for a QD-based LWIR photodetector operating at room temperature and only one order of magnitude lower than cooled devices [56, 57]. This result is even more remarkable considering the presence of a single layer of 0D-2D nanostructure in the device.

VI. CONCLUSIONS

In this work we have presented an innovative approach to long wavelength IR detection based on resonant states absorption in QDs. By deeply analyzing QDIP working principles we devised a quantum nanostructure whose electronic states have been engineered in order to exploit absorption transitions towards resonant states in the the continuum to massively enhance the extraction of photoexcited carriers. This innovative approach allowed us also to promote carrier capture and thermalization, while preventing thermionic emission from the QD ground states at room temperature. For this purpose we realized a hybrid 0D-2D nanostructure made of GaAs and embedded in an Al_{0.3}Ga_{0.7}As barrier layer with optimized QW thickness and QD shape

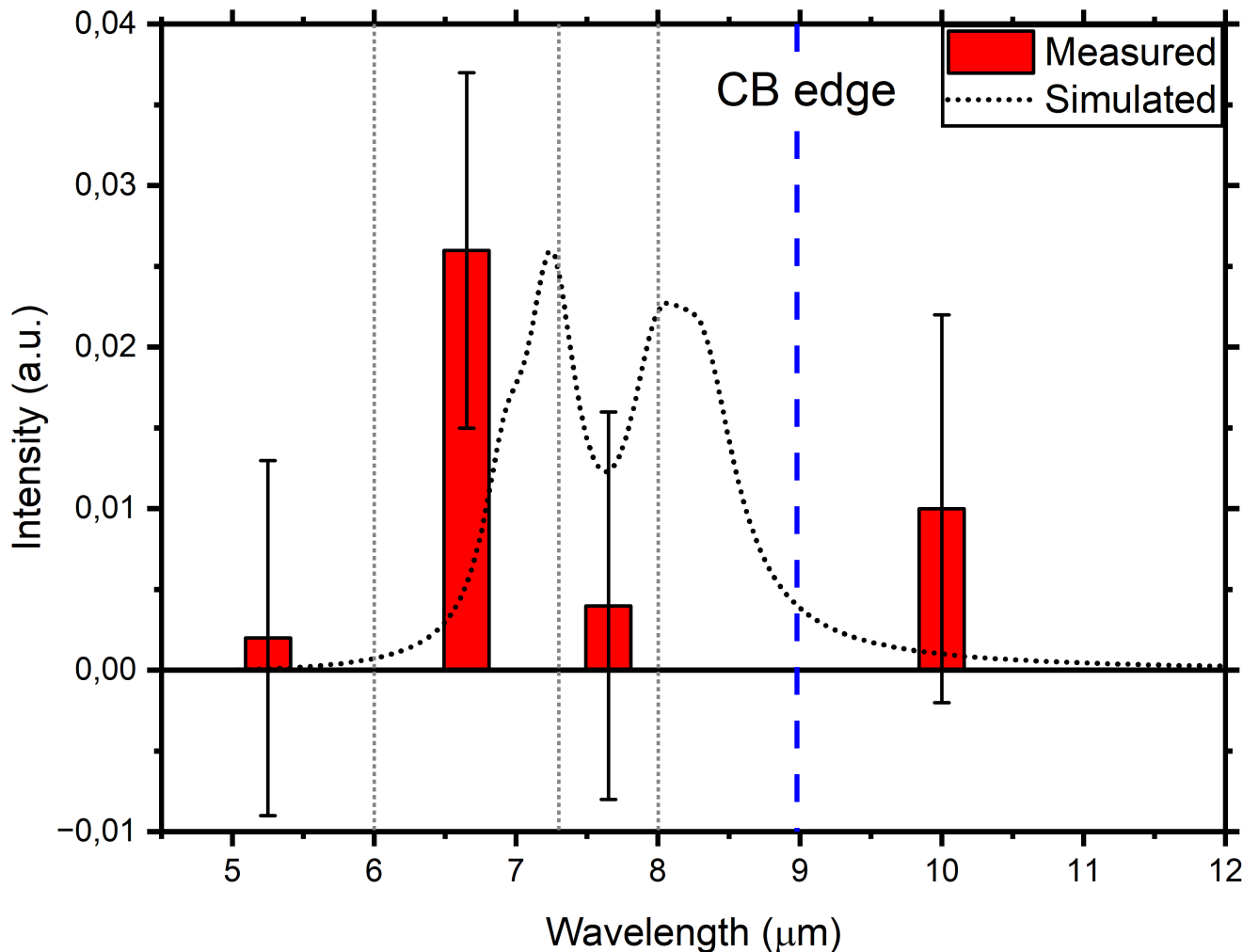


Figure 8. Comparison between the room temperature simulated IR absorption spectrum and the measured one. The dashed line indicates the offset between the electron ground state and the $\text{Al}_{0.3}\text{Ga}_{0.7}\text{As}$ CB edge.

and size. We realized such a device using the droplet epitaxy technique which allow for such a high degree of flexibility.

The QDIPs realized using our design show a high room temperature detectivity of $9.8 \times 10^9 \text{ cm Hz}^{1/2}/\text{W}$ at -4 V peaked in the $6 \mu\text{m} - 7.3 \mu\text{m}$ range, thus demonstrating a remarkable agreement between the theoretical predictions and the experimental measurements. These figures show that the significant advantages in sensitivity and tunability of QDIPs can be brought to room temperature operation, thus realizing their full potential in various applications. Expanding into emerging markets and integrating with complementary technologies could present opportunities for the the growth and innovation in the LWIR sensor market in the future.

As a final remark, these results demonstrate the enormous potential of resonant states absorption in quan-

tum dots, which is entirely unexplored up to date. With this work we are opening a new path for infrared photodetectors, which we believe will have a groundbreaking impact on many branches of optoelectronics.

VII. METHODS

A. Growth

The sample was grown on a 2" GaAs undoped wafer inside a Molecular Beam Epitaxy chamber provided with As valved cracked cell. The growth started with the deposition of $1 \mu\text{m}$ of Si doped GaAs as lower contact, followed by 350 nm of $\text{Al}_{0.3}\text{Ga}_{0.7}\text{As}$ barrier layer deposited at 650°C and a 1.1 nm Si doped GaAs QW. The quantum dots were fabricated on the top of the quantum well using droplet epitaxy. The substrate

temperature was lowered to 150°C and 3 MLs of Ga were deposited with a rate of 0.1 ML/s and a background pressure lower than 2×10^{-9} torr. At the same temperature As valve was open to crystallize the Ga droplets with a beam equivalent pressure of 5×10^{-5} torr. The quantum dots were covered with 20 MLs of $\text{Al}_{0.3}\text{Ga}_{0.7}\text{As}$ deposited by migration enhanced epitaxy at 400°C and annealed for 5 minutes at this temperature to improve the crystalline quality. The detector structure was completed with 350 nm of $\text{Al}_{0.3}\text{Ga}_{0.7}\text{As}$ and 500 nm of Si doped GaAs as upper contact, deposited at 650°C.

B. Device fabrication

The wafer was then processed in clean-room environment with photolithography and wet-etching process in order to create mesas and finally metal contacts were deposited in evaporation chamber. Mesa etching was done by a wet approach, using an $\text{H}_3\text{PO}_4 : \text{H}_2\text{O}_2 : \text{H}_2\text{O}$ solution with 1:2.5:8 relative concentrations. Metal contacts were deposited by e-beam evaporation using a stack of 122 nm Cu and 78 nm Ge and annealed in nitrogen atmosphere at 420°C C for 10 minutes, in order to get ohmic contacts. The mesa area was 0.09 cm^2 .

C. Photoabsorption

Photoabsorption measurements were performed on a dedicated system composed by an infrared source operating at 900°C, a parabolic mirror and a plane-convex ZnSe lens to focus the infrared radiation, a chopper and a set of optical longpass filters at 4.5, 6 and 7.3 μm and a bandpass between 8 and 12 μm). The sample was connected to a voltage generator, a transimpedance amplifier with a fixed gain of 10^6 A/V and a lock-in amplifier. For each filter we measured the output signal performing a sweep between -4 and 0 volts, obtaining an I-V characteristics from which we calculated the resistance of the detector under IR radiation. When using longpass filters, the resulting values include the contributions from longer wavelengths. Therefore, we determined the change in resistance in each spectral window by subtracting the results obtained with two subsequent filters. This value is inversely proportional to the photogenerated current.

D. AFM

The sample morphology was analyzed at room temperature by the Veeco Innova atomic force microscope

(AFM) in tapping mode using Nanosensors SSS-NCHR sharp silicon tips capable of a lateral resolution of about 2 nm. The AFM images were then processed and analyzed with the software Gwyddion [58]. The QDs (i.e. grains) were then identified by defining a height threshold in the image. Their equivalent radius was obtained by measuring the width of the grains at the intersection with the threshold. Their height was obtained by subtracting the median height of the background after subtracting the grains to the maximum value of each grain.

E. Numerical simulations

The numerical simulations of the quantum properties of the nanostructures were performed using TiberCAD [59]. The calculations were performed using a finite elements method, modeling the nanostructures based on the geometrical parameters obtained from the analysis of AFM images (figure 6). The QD shape was assumed to be a truncated cone, as described in a previous work of Bietti et al. [60], with an height of 2.0 nm and a major radius of 9.5 nm. The band structure was obtained by solving single-electron drift diffusion equations including Pikus-Bir strain corrections. The quantum states were then computed in the structure by using the k-p model with an eight band envelope function approximation. Finally, the intraband transitions were studied by computing the optical matrix elements of the transitions in the dipole approximation, as defined in the equation:

$$|M|_{fi}^2 = |\langle \Psi_f | \mathbf{P} \cdot \hat{e} | \Psi_i \rangle|^2 \quad (3)$$

where $\Psi_{f,i}$ are the envelope functions of the final and initial state respectively, $\mathbf{P} = -i\hbar\nabla$ is the photon momentum operator and \hat{e} is the polarization versor [61]. In our setup, where the IR light was incident perpendicularly on the surface of the detector, only the in-plane polarization components are taken into account. Materials parameters for the simulations were taken from Vurgaftman et al.[62].

F. Photoluminescence

For the photoluminescence measurement a continuous-wave mode solid-state laser with a wavelength of 532 nm was used. For the detection, an Ocean Optics USB2000+ spectrometer with a focal length of 42 mm for input and 68 mm for output was used. The temperature was controlled by using a closed-cycle He cryostat.

VIII. ACKNOWLEDGEMENT

We acknowledge support from MUSA – Multilayered Urban Sustainability Action – project (ECS 000037), funded by the European Union – NextGenerationEU, under the National Recovery and Resilience Plan (NRRP) Mission 4 Component 2 Investment Line 1.5: Strengthening of research structures and creation of R&D “innovation ecosystems”, set up of “territorial leaders in R&D”

IX. AUTHOR CONTRIBUTIONS

S.V. and S.B. performed the simulations. S.B., A.T. and A.F. carried out the growth and performed the AFM measurements. S.A. and T.K. performed PL measurements and analysis. S.B. performed the photoabsorption measurements. S.V., S.B. and S.S. have conceived the idea. All authors contributed to the data

analysis and to the writing of the paper.

X. COMPETING INTERESTS

The authors declare no competing interests.

XI. CORRESPONDENCE

Correspondence and requests for materials should be addressed to Stefano Vichi.

XII. DATA AVAILABILITY

The data that support the findings of this study are available from the corresponding author upon reasonable request.

-
- [1] Sobrino, J. A. & Jiménez-Muñoz, J. C. Minimum configuration of thermal infrared bands for land surface temperature and emissivity estimation in the context of potential future missions **148**, 158–167. URL <http://dx.doi.org/10.1016/j.rse.2014.03.027>. ISBN: 00344257 Publisher: Elsevier Inc.
- [2] Cao, B. *et al.* A review of earth surface thermal radiation directionality observing and modeling: Historical development, current status and perspectives **232**, 111304. URL <https://linkinghub.elsevier.com/retrieve/pii/S0034425719303232>.
- [3] Zhang, Y., Carballo, A., Yang, H. & Takeda, K. Perception and sensing for autonomous vehicles under adverse weather conditions: A survey **196**, 146–177. URL <https://linkinghub.elsevier.com/retrieve/pii/S0924271622003367>.
- [4] Rogalski, A. Optical detectors for focal plane arrays **12**.
- [5] Rogalski, A., Antoszewski, J. & Faraone, L. Third-generation infrared photodetector arrays **105**.
- [6] Ren, A., Yuan, L., Xu, H., Wu, J. & Wang, Z. Recent progress of III–v quantum dot infrared photodetectors on silicon **7**, 14441–14453. URL <https://pubs.rsc.org/en/content/articlelanding/2019/tc/c9tc05738b>. Publisher: The Royal Society of Chemistry.
- [7] Kim, H. *et al.* InAs/GaAs quantum dot infrared photodetector on a si substrate by means of metal wafer bonding and epitaxial lift-off **25**, 17562–17570. URL <https://opg.optica.org/oe/abstract.cfm?uri=oe-25-15-17562>. Publisher: Optica Publishing Group.
- [8] Bietti, S. *et al.* Fabrication of high efficiency III–v quantum nanostructures at low thermal budget on si **95**.
- [9] Cavigli, L. *et al.* High temperature single photon emitter monolithically integrated on silicon **100**.
- [10] Bietti, S. *et al.* Monolithic integration of optical grade GaAs on si (001) substrates deeply patterned at a micron scale **103**.
- [11] Ballabio, A. *et al.* GaAs epilayers grown on patterned (001) silicon substrates via suspended ge layers **9**, 1–8. [_eprint: 31772248](https://arxiv.org/abs/31772248) [_eprinttype: pmid](https://pubs.aip.org/jap/article/92/10/5982/757934/One-and-two-phonon-capture-processes-in-quantum).
- [12] Zeng, C., Fu, D., Jin, Y. & Han, Y. Recent progress in III–v photodetectors grown on silicon **10**, 573. URL <https://www.mdpi.com/2304-6732/10/5/573>. Number: 5 Publisher: Multidisciplinary Digital Publishing Institute.
- [13] Magnusdottir, I., Uskov, A. V., Bischoff, S., Tromborg, B. & Mørk, J. One- and two-phonon capture processes in quantum dots **92**, 5982–5990. URL <https://pubs.aip.org/jap/article/92/10/5982/757934/One-and-two-phonon-capture-processes-in-quantum>.
- [14] Müller, T., Schrey, F. F., Strasser, G. & Unterrainer, K. Ultrafast intraband spectroscopy of electron capture and relaxation in InAs/GaAs quantum dots **83**, 3572–3574. ISBN: 00036951.
- [15] Ryzhii, V. The theory of quantum-dot infrared phototransistors **11**, 759–765.
- [16] Ryzhii, V., Khmyrova, I., Mitin, V., Stroschio, M. & Willander, M. On the detectivity of quantum-dot infrared photodetectors **78**, 3523–3525. URL <https://pubs.aip.org/apl/article/78/22/3523/113839/On-the-detectivity-of-quantum-dot-infrared>.
- [17] Höglund, L. *et al.* Optical pumping as artificial doping in quantum dots-in-a-well infrared photodetectors **94**.
- [18] Ramiro, I. *et al.* Optically triggered infrared photodetector **15**, 224–228. [_eprint: 25490236](https://arxiv.org/abs/25490236) [_eprinttype: pmid](https://pubs.aip.org/jap/article/15/2/224/148144).

- [19] Vichi, S. *et al.* Optically controlled dual-band quantum dot infrared photodetector **12**, 1–6. URL <https://doi.org/10.1177/18479804221085790>. ISBN: 1847980422, 2103.03582.
- [20] Wolde, S. *et al.* Noise, gain, and capture probability of p-type InAs-GaAs quantum-dot and quantum dot-in-well infrared photodetectors **121**. URL <http://dx.doi.org/10.1063/1.4989834>.
- [21] Krishna, S. Quantum dots-in-a-well infrared photodetectors **47**, 153–163. ISBN: 0022-3727.
- [22] Barve, A. V. *et al.* Barrier selection rules for quantum dots-in-a-well infrared photodetector **48**, 1243–1251.
- [23] Koguchi, N., Takahashi, S. & Chikyow, T. New MBE growth method for InSb quantum well boxes **111**, 688–692. URL <https://linkinghub.elsevier.com/retrieve/pii/002202489191064H>.
- [24] Kim, J. S., Han, I. S., Lee, S. J. & Song, J. D. Droplet epitaxy for III-v compound semiconductor quantum nanostructures on lattice matched systems **73**, 190–202. URL <https://doi.org/10.3938/jkps.73.190>.
- [25] Basso Basset, F. B. *et al.* Spectral broadening in self-assembled GaAs quantum dots with narrow size distribution **126**. Publisher: AIP Publishing LLC.
- [26] Bietti, S., Somaschini, C. & Sanguinetti, S. Crystallization kinetics of ga metallic nano-droplets under as flux **24**.
- [27] Sablon, K. A., Lee, J. H., Wang, Z. M., Shultz, J. H. & Salamo, G. J. Configuration control of quantum dot molecules by droplet epitaxy **92**, 203106. URL <https://doi.org/10.1063/1.2924308>.
- [28] Heyn, C., Stemann, A., Schramm, A. & Hansen, W. Droplet epitaxy of GaAs quantum dots on (001), vicinal (001), (110), and (311)a GaAs **311**, 1825–1827. URL <https://www.sciencedirect.com/science/article/pii/S0022024808011561>.
- [29] Tuktamyshev, A. *et al.* Nucleation of ga droplets self-assembly on GaAs(111)a substrates **11**, 1–11. URL <https://doi.org/10.1038/s41598-021-86339-3>. ISBN: 0123456789 Publisher: Nature Publishing Group UK _eprint: 33767304 _eprinttype: pmid.
- [30] Barbiero, A. *et al.* Exciton fine structure in InAs quantum dots with cavity-enhanced emission at telecommunication wavelength and grown on a GaAs (111) a vicinal substrate **18**, 1–8.
- [31] Sanguinetti, S. *et al.* Modified droplet epitaxy GaAs/AlGaAs quantum dots grown on a variable thickness wetting layer **253**, 71–76.
- [32] Steinhoff, A. *et al.* Combined influence of coulomb interaction and polarons on the carrier dynamics in In-GaAs quantum dots **88**, 205309. URL <https://link.aps.org/doi/10.1103/PhysRevB.88.205309>.
- [33] Scaccabarozzi, A. *et al.* Enhancing intermediate band solar cell performances through quantum engineering of dot states by droplet epitaxy 1–8.
- [34] Sanguinetti, S., Gurioli, M., Watanabe, K., Tateno, T. & Koguchi, N. Dependence of quantum dot auger carrier relaxation on barrier dimensionality: An experimental study **19**, S293–S295. URL <http://stacks.iop.org/0268-1242/19/i=4/a=098?key=crossref.ae9900be21d36192aaadd5f4113c74b2>.
- [35] Luque, A. *et al.* Experimental analysis of the quasi-fermi level split in quantum dot intermediate-band solar cells **87**. ISBN: 0003-6951.
- [36] Toda, Y., Moriwaki, O., Nishioka, M. & Arakawa, Y. Efficient carrier relaxation mechanism in InGaAs/GaAs self-assembled quantum dots based on the existence of continuum states **82**, 4114–4117. URL <https://link.aps.org/doi/10.1103/PhysRevLett.82.4114>.
- [37] Ferreira, R. & Bastard, G. Carrier capture and intradot auger relaxation in quantum dots **74**, 2818. ISBN: 00036951 (ISSN).
- [38] H. C. Liu. Dependence of absorption spectrum and responsivity on the upper state position in quantum well intersubband photodetectors **73**, 3062–3067.
- [39] Ikončić, Z., Milanović, V. & Tjapkin, D. Bound-free intraband absorption in GaAs-al \emph{x} gal- \emph{x} as semiconductor quantum wells **54**, 247–249. URL <https://pubs.aip.org/apl/article/54/3/247/55714/Bound-free-intraband-absorption-in-GaAs-AlxGa1-xAs>.
- [40] Hsu, C. W., Zhen, B., Stone, A. D., Joannopoulos, J. D. & Soljacic, M. Bound states in the continuum **1**.
- [41] Azzam, S. I. & Kildishev, A. V. Photonic bound states in the continuum: From basics to applications **9**, 16–24.
- [42] Bogdanov, A. A. *et al.* Bound states in the continuum and fano resonances in the strong mode coupling regime **1**, 016001. URL <https://www.spiedigitallibrary.org/journals/advanced-photonics/volume-1/issue-1/016001/Bound-states-in-the-continuum-and-Fano-resonances-in-the-10.1117/1.AP.1.1.016001.full>. Publisher: SPIE.
- [43] Joseph, S., Pandey, S., Sarkar, S. & Joseph, J. Bound states in the continuum in resonant nanostructures: An overview of engineered materials for tailored applications **10**, 4175–4207. URL <https://www.degruyter.com/document/doi/10.1515/nanoph-2021-0387/html>. Publisher: De Gruyter.
- [44] Fang, C. *et al.* High-*Q* resonances governed by the quasi-bound states in the continuum in all-dielectric metasurfaces **4**, 200030–200030. URL <http://www.oejournal.org/article/doi/10.29026/oea.2021.200030>.
- [45] Romano, S. *et al.* Ultrasensitive surface refractive index imaging based on quasi-bound states in the continuum **14**, 15417–15427. URL <https://doi.org/10.1021/acsnano.0c06050>. Publisher: American Chemical Society.
- [46] Yang, F. *et al.* Bending sensing based on quasi bound states in the continuum in flexible terahertz metasurface **11**, 2300909. URL <https://onlinelibrary-wiley-com.unimib.idm.oclc.org/doi/abs/10.1002/adom.202300909>. _eprint: <https://onlinelibrary-wiley.com/doi/pdf/10.1002/adom.202300909>.
- [47] Luque, A. *et al.* Absorption coefficient for the intraband transitions in quantum dot materials: Absorption coefficient for the intraband transitions $n/a-n/a$. URL <https://onlinelibrary-wiley.com/doi/10.1002/pip.1250>.
- [48] Wang, S. Y., Lin, S. D., Wu, H. W. & Lee, C. P. Low dark current quantum-dot infrared photodetectors with an AlGaAs current blocking layer **78**, 1023–1025. ISBN:

- 0003-6951 _eprint: 166983500001 _eprinttype: pmid.
- [49] Jiang, L. *et al.* In 0.6 ga 0.4 as/GaAs quantum-dot infrared photodetector with operating temperature up to 260 k **82**, 1986–1988. URL <https://pubs.aip.org/apl/article/82/12/1986/513808/In0-6Ga0-4As-GaAs-quantum-dot-infrared>.
- [50] Chakrabarti, S. *et al.* High-performance mid-infrared quantum dot infrared photodetectors **38**, 2135–2141. URL <https://iopscience.iop.org/article/10.1088/0022-3727/38/13/009>.
- [51] Chen, W. *et al.* Demonstration of InAs/InGaAs/GaAs quantum dots-in-a-well mid-wave infrared photodetectors grown on silicon substrate **36**, 2572–2581. URL <https://ieeexplore.ieee.org/document/8309403/>.
- [52] Ghadi, H. *et al.* Optimizing dot-in-a-well infrared detector architecture for achieving high optical and device efficiency corroborated with theoretically simulated model **751**, 337–348. URL <https://linkinghub.elsevier.com/retrieve/pii/S0925838818312866>.
- [53] Billaha, A. & Das, M. K. Influence of doping on the performance of GaAs/AlGaAs QWIP for long wavelength applications **24**, 25–33. URL <https://www.degruyter.com/document/doi/10.1515/oere-2016-0006/html>. Publisher: De Gruyter.
- [54] Pavesi, L. & Guzzi, M. Photoluminescence of AlxGa1-xAs alloys **75**, 4779–4842.
- [55] Martyniuk, P. & Rogalski, A. Quantum-dot infrared photodetectors: Status and outlook **32**, 89–120. URL <http://linkinghub.elsevier.com/retrieve/pii/S0079672708000190>.
- [56] Rogalski, A. Progress in quantum dot infrared photodetectors. In Tong, X., Wu, J. & Wang, Z. M. (eds.) *Quantum Dot Photodetectors*, 1–74 (Springer International Publishing). URL https://doi.org/10.1007/978-3-030-74270-6_1.
- [57] Xue, X. *et al.* High-operating-temperature mid-infrared photodetectors via quantum dot gradient homojunction **12**, 2. URL <https://www.nature.com/articles/s41377-022-01014-0>. Publisher: Nature Publishing Group.
- [58] Nečas, D. & Klapetek, P. Gwyddion: an open-source software for SPM data analysis **10**, 181–188. URL <https://www.degruyter.com/document/doi/10.2478/s11534-011-0096-2/html>. Publisher: De Gruyter Open Access.
- [59] See www.tiberlab.com for TiberCAD software. URL [Seewww.tiberlab.com](http://www.tiberlab.com)forTiberCADsoftware.
- [60] Bietti, S. *et al.* Precise shape engineering of epitaxial quantum dots by growth kinetics **92**, 075425. URL <http://link.aps.org/doi/10.1103/PhysRevB.92.075425>.
- [61] Harrison, P. & Valavanis, A. *Quantum Wells, Wires and Dots: Theoretical and Computational Physics of Semiconductor Nanostructures* (Wiley), fourth edition edn.
- [62] Vurgaftman, I., Meyer, J. R. & Ram-Mohan, L. R. Band parameters for III-v compound semiconductors and their alloys **89**, 5815–5875. ISBN: 0021-8979 _eprint: 9948405 _eprinttype: pmid.